Unraveling the control of reversibility for actuators based on cellulose nanofibers

Lisa Lopes da Costa, Céline Moreau, Denis Lourdin, Bernard Cathala, Ana Villares

Unraveling the control of reversibility for actuators based on cellulose nanofibers

Lisa Lopes da Costa,* Céline Moreau, Denis Lourdin, Bernard Cathala, Ana Villares

UR1268 BIA, INRAE, F-44316 Nantes, France

*lisa.lopes-da-costa@inrae.fr

Abstract

In this work, we have prepared cellulose-based actuators taking advantage of the pH-sensitive solubility of chitosan (CH) and the mechanical strength of CNFs. Bilayer films were prepared by vacuum filtration inspired by plant structures that exhibit reversible deformation under pH changes. The presence of CH in one of the layers led to asymmetric swelling at low pH, thanks to the electrostatic repulsion between charged amino groups of CH, and the subsequent twisting with the CH layer on the outside. Reversibility was achieved by substituting pristine CNFs with carboxymethylated CNFs (CMCNFs), that are charged at high pH and thus competed with the effects of amino groups. Swelling and mechanical properties of layers under pH changes were studied by gravimetry and dynamic mechanical analysis (DMA) to quantify the contribution of chitosan and the modified CNFs on the reversibility control. This work evidenced the key role of surface charge and layer stiffness to achieve reversibility. Bending was triggered by the different water uptake of each layer, and shape recovery was achieved when the shrunk layer shower higher rigidity than the swollen layer.

Keywords

Cellulose films; chitosan; pH-responsive; programmable; carboxymethylation; dynamic mechanical analysis

1. Introduction

Actuators are hierarchical structures that undergo shape changes triggered by external stimuli, such as temperature, light, humidity, or pH. These materials respond to the current demand for engineering multifunctional assemblies that adapt to their environment, as similarly observed in Nature (Erb et al., 2013; Ganewatta et al., 2021; Rüggeberg & Burgert, 2015; Y. Wang et al., 2020). By actuation, biological systems such as the pinecones or wild wheat awns release their seeds in response to humidity uptake and associated cell wall swelling, which guarantees plant survival (Dawson et al., 1997; Elbaum et al., 2007). Nature is therefore a source of inspiration for the fabrication of actuators triggered by water swelling, and over the last few years, the use of natural polymers has shown a growing interest in the scientific community. Among the myriad of natural polymers, cellulose nanofibers (CNFs) revealed a great potential for this purpose (Chen et al., 2022; Liu et al., 2021). CNFs have been used for decades in the papermaking industry, coatings, optical films, foodstuffs, pharmaceutics, and cosmetics (Abdul Khalil et al., 2012; Y. Zhang et al., 2013). CNFs are obtained by mechanical lamination of the cellulose fiber, and the fibrillation to the nanometer scale provides attractive properties, including high aspect ratio, high strength and stiffness, low density, transparency, high hydrophilicity, high surface area, and low thermal expansion (Dufresne, 2013; Eichhorn et al., 2010; Moon et al., 2011). Furthermore, cellulose is highly abundant and biodegradable, which makes it an excellent candidate to fabricate novel materials (Huber et al., 2011). One of the main drawbacks of cellulose in the fabrication of materials is the interaction with water due to the presence of a high number of hydroxyl groups in the cellulose chain (Kuang et al., 2019; M. Wang et al., 2015; Wei et al., 2021; Yang et al., 2021; L. Zhang et al., 2016). The water uptake is the main cause of the low stability of cellulose materials, with a substantial loss of mechanical properties. Nevertheless, the cellulose-water interaction can be exploited to design cellulose-based water-responsive actuators. By carefully designing multilayered structures with different functionalities in each layer, water uptake can be controlled to display asymmetrical expansion of the layers, and therefore to perform actuation. Indeed, the hydroxyl groups along the skeleton of cellulose enable to extend CNF versatility by chemical modification resulting in “tailor-made” specific properties (Habibi, 2014).

In previous studies, we prepared pH-responsive bilayer films based on functionalized CNFs (Chemin et al., 2020). The first layer contained carboxylated CNFs and the second layer was composed of aminated CNFs. When the film was subjected to high pH, the deprotonation of carboxylic acid groups caused electrostatic repulsion between the negative charges, which facilitated water adsorption. Therefore, the different water uptake and expansion of the negatively charged carboxylated layer compared to the aminated layer resulted in film bending. Then, the inverse mechanism was obtained at low pH because of the protonation of the aminated layer, which adsorbed more water by a similar mechanism. Despite the controlled bending at high and low pH, the actuation of these bilayer films was not reversible, and the film remained bent when it returned to the initial conditions. Therefore, in this work, we focused on the interaction between water and the functional groups grafted on the cellulose surface to understand the mechanism of actuation, and the parameters required to achieve reversibility.

We succeed in fabricating a new bilayer actuator displaying reversible shape-changing under pH variation. First, CNFs were combined with chitosan (CH) to form a pH-sensitive film (CH-CNF) with promising mechanical properties by physical interlocking between CH and CNF networks without chemical cross-linkers. CH protonates in acid environments due to the formation of non-bonding pairs of electrons in amino groups, allowing its solubilization. Above pK_a of 6.5, approximatively, CH chains at their neutral form associate together and consequently aggregate (Rosca et al., 2005; Vleugels et al., 2018). Hence, CH can be considered for designing responsive structures thanks to its

pH-dependent solubility properties. We studied the behavior of CH-CNF films in terms of adsorption of CH on CNFs, polymer amount and distribution, and pH-associated structural changes. In the second stage, we fabricated bilayer actuator films by combining CH-CNF layers with CNF-based layers (non-modified or carboxymethylated) and we monitored the actuator properties in terms of swelling and mechanical properties. This work presents polysaccharide actuators fabricated by their tailored combination and provides a better understanding of the polysaccharide-water interactions that gives more insight into the requirements to achieve reversible actuation.

2. Materials and Methods

2.1. Materials

CNFs Exilva P 01-V (10% w/v) were kindly provided by Borregaard (Sarpsborg, Norway). Chitosan (medium molecular weight, 75-85 % deacetylated) (CH), monochloroacetic acid (MCA), hydrochloric acid (HCl), rhodamine B isothiocyanate (RBITC), and sodium hydroxide (NaOH) were purchased from Sigma Aldrich. Dimethyl sulfoxide (DMSO) was purchased from Merck, isopropanol from VWR, and poly(allylamine hydrochloride) (PAH) from Polysciences. A Spectra/Por dialysis membrane, MWCO 12–14,000 Da, was purchased from Spectrum Laboratories Inc, and polyvinylidene fluoride (PVDF) membranes (pore size 0.22 µm, diameter 47 mm) from Merck. Water was purified by the Millipore Milli-Q purification system (18.2 MΩ).

2.2. Fluorescence labeling of chitosan (CH)

A CH solution was prepared at 1% (*w/v*) in 0.1 M HCl. Then, RBITC, dissolved in 20 mL of DMSO, was added to the CH solution. The reaction was stirred for 3 h, in dark, at room temperature. RBITC-labelled chitosan (RBITC-CH) was precipitated by addition of NaOH. RBITC-CH was purified by centrifugation until no free RBITC was detected in supernatant. RBITC-CH was solubilized at 1 % (*w/v*) in 0.1 M HCl and dialyzed against ultra-pure water for 3 days in dark.

2.3. Carboxymethylation

Carboxymethylated CNFs (CMCNFs) were synthesized by the reaction between hydroxyl groups and MCA, as previously described (Lopes da Costa et al., 2023). CNFs (500 mg) were impregnated with MCA dissolved in isopropanol. Two MCA/anhydroglucose (AGU) molar ratios were performed (0.50 and 0.70) to achieve different degrees of substitution (DS). In parallel, NaOH was dissolved in isopropanol at 60°C for 1 h. Impregnated CNFs were added to the NaOH solution and the mixture was stirred at 70°C for 1 h. The resultant CNFs were purified by filtration through PVDF membranes with ultra-pure water, then 0.1 M HCl, and finally ultra-pure water.

2.4. Film fabrication

Cellulose films were fabricated by Büchner filtration through PVDF membranes. Before filtration, all polymer dispersions (CNFs, CH-CNF mixture, and CMCNFs) were prepared at 2.5 $g \cdot L^{-1}$. For the single-layer films, the dispersion was poured into the membrane and filtrated for 30 min under 50 mbar at room temperature. For the bilayer films, after filtrating the first dispersion, the second dispersion was added to the first layer and filtrated again under the same conditions. All films were, then, dried between Whatman filter paper under a weight of 500 g for 48 h at room temperature. Afterward, the disc-shaped films (diameter = 36 mm) were weighted and their thickness was measured with a Mitutoyo digimatic micrometer. The density (*d*) was calculated as represented below:

$$d = \frac{m}{\pi r^2 t} \quad (1)$$

where *m*, *r*, and *t* are respectively the weight, radius, and thickness of the dried films.

The films were then cut into different shapes depending on the conducted analysis; rectangles (6 x 24 mm^2) for actuation tests (2.5.6) and dynamic mechanical analysis (2.5.8) and squares (24 x 24 mm^2) for swelling ratio quantification (2.5.7).

2.5. Characterization

2.5.1. Quartz crystal microbalance with dissipation monitoring (QCM-D)

QCM-D equipment (E4, Q-Sense instrument, AB, Sweden) using a piezoelectric AT-cut quartz crystal coated with gold electrodes on each side (QSX301, Q-Sense) was employed to assess the adsorption of CH on CNFs. The quartz crystals, cleaned in a piranha bath for 5 min, were set up into the cells and ultra-pure water was injected at a flow rate of 0.1 $mL \cdot min^{-1}$ at 20 °C for at least 1 h until reaching a stable baseline. A PAH solution (0.1 $g \cdot L^{-1}$) was first injected for 15 min before the adsorption of biopolymers. Then, CNF dispersion (0.1 $g \cdot L^{-1}$) and CH solution (0.2 $g \cdot L^{-1}$, pH 1) were successively injected into the cells for 15 and 20 min respectively. A rinsing step with Milli-Q water or 0.1 M HCl was done before the subsequent injection of polymer solutions.

Frequency ($\Delta f_n/n$) and dissipation ($\Delta D_n/n$) changes were simultaneously registered at 5 MHz fundamental resonance frequency and its several overtones as a function of time. ($\Delta f_n/n$) can be related to the hydrated mass of the adsorbed polymers while ($\Delta D_n/n$) provides information about conformational changes and softness/rigidity of the system studied. QCM-D experiments were carried out at least twice. The third overtone (15 MHz) was used in the evaluation of the QCM-D data.

2.5.2. Attenuated total reflection Fourier transform infrared (ATR-FTIR) spectroscopy

ATR-FTIR spectra were recorded with a Nicolet iS50 FTIR spectrometer (Thermo Fisher, Waltham, Massachusetts, USA) with the accumulation of 200 scans between 800 and 4000 cm^{-1} with a resolution of 4 cm^{-1}. The single-layer films composed of CNFs, CH-CNF, or CH were analyzed. A band decomposition of CH film spectra was performed in the 1800-1500 cm^{-1} region to determine the exact positions of the peak related to C=O stretching from amide I and the two peaks associated with N-H deformation. OriginPro 8.5 software was used for the band decomposition. The spectrum was first normalized with the peak at 1150-1085 cm^{-1} (ether bonding) with a linear baseline made by interpolation. The decomposition was done in Gaussian peaks with the minimum number of peaks and was considered valuable when $R \geq 0.99$. For CH-CNF spectra, the characteristics of the peak at 1536 cm^{-1} (N-H deformation) were measured to follow the CH amount in CH-CNF films (wavenumber, area, full width at half maximum, and area contribution). The spectra were also normalized with the peak at 1150-1085 cm^{-1} with a linear baseline made by interpolation.

2.5.3. Elementary analysis

To quantify the percentage of CH in the CH-CNF films, the atomic composition (carbon, hydrogen, and nitrogen content) of freeze-dried CNFs, single-layer CH and CH-CNF films was determined using a Thermo Fischer Scientific Elemental Analyzer (Model Flash 2000). Each sample was measured twice.

2.5.4. Confocal laser scanning microscopy (CLSM)

Single-layer films containing RBITC-CH and CNF (weight ratio 1:4) were observed by confocal microscopy (Leica TCS-SP2) to visualize the distribution of CH within the film. Confocal images were acquired with a LSM-510 UV-Vis microscope equipped with 63 × 1.2 water immersion objectives (Zeiss, Germany). Excitation/emission wavelengths were 530/566 nm.

2.5.5. Conductometric titration

CMCNFs (20 mg) were firstly acidified with HCl (0.1 M) and titrated with NaOH (0.1 M) by a TIM900 titration manager (Metrohm). The conductivity was measured simultaneously during the titration by a CDM749 conductivity cell.

The degree of substitution (DS) was calculated as (Abitbol et al., 2013; Beck et al., 2015):

$$DS = \frac{162(V_{eq2}-V_{eq1})C_{NaOH}}{m-M(V_{eq2}-V_{eq1})C_{NaOH}} \qquad (2)$$

Where V_{eq1} and V_{eq2} are the equivalence volumes of NaOH (L), C_{NaOH} is the concentration of NaOH (mol·L^{-1}), m is the dried weight of CNFs (g), M is the molecular weight of the carboxymethyl group, and 162 is the molecular weight of AGU (g·mol^{-1}).

2.5.6. Actuation tests

Actuation was monitored by immersing the bilayer films under different pH conditions (acidic, neutral, and basic). Bilayer films were cut into rectangles (24 x 6 mm^2) and were fixed in a clamp that was held by a stand. A glass vessel containing 0.01 M HCl (pH 2), Milli-Q water, or 0.01 M NaOH (pH 12) was placed on the moveable platform. Then, a SVS-vistek EXO camera and the camera software from BIA unit were used to capture the film movement. Therefore, the moveable platform was driven up to dip the bilayer film into the liquid in the glass vessel and start the actuation test. The test steps were the following: the bilayer films were first immersed for 10 min in 0.01 M NaOH, then 5 min in 0.01 HCl, and 20 min in 0.01 M NaOH. Each actuation test was repeated three times.

2.5.7. Swelling ratio quantification

Disc-shaped films were cut into squares of 24 x 24 mm^2. The dry films were weighed, then immersed in Milli-Q water, or aqueous solutions of 0.01 M HCl (pH 2) or 0.01 M NaOH (pH 12) for 1 min and weighed again. The swelling ratio expressed as the weight of absorbed water per the weight of the dry film (SW) was calculated following this equation:

$$SW = \frac{(m_w-m_d)}{m_d} \qquad (3)$$

where m_w and m_d are respectively the weight of the wet and dry film (mg).

Each sample was measured five times.

2.5.8. Dynamic mechanical analysis (DMA)

The dynamic mechanical properties as a function of pH for CNF, CH-CNF, or CMCNF films were determined with a Dynamic Mechanical Analyser (DTMA MkIV, Rheometric Scientific, US). The DMA system was flipped from bottom to top in order to measure the samples immersed in pH-controlled aqueous solutions at 20°C. Tests were conducted on rectangular-shaped strip samples (10×6 mm^2) in the tensile mode with a dynamic strain amplitude of 0.1%, and a constant load force of 0.1 N. Recordings of the specimens were taken following this procedure: 10 min air equilibrium, then 10 min immersion in the liquid (HCl 0.01 M, Milli-Q water, or NaOH 0.01M).

3. Results and discussion

3.1. Structure and pH-sensitive behavior of chitosan-cellulose films (CH-CNF)

In this work, we took advantage of the pH-responsive properties of chitosan (CH) to fabricate all-polysaccharide actuators. CH contains amino groups that make the polymer pH-responsive. In acidic conditions, the charged amino groups favor the hydration and dissolution of CH chains due to the higher hydrophilicity and electrostatic repulsion between the positive charges. Above its pK_a (~ 6), the neutralization of the amino groups drives CH aggregation by the association between the CH chains (Rosca et al., 2005; Vleugels et al., 2018). However, CH-based actuators require cross-linking of the polysaccharide chains, to avoid the dissolution of CH at low pH. Therefore, in this work, CH was combined with cellulose nanofibers (CNFs) to form a physically cross-linked network within the film. The first step was therefore to demonstrate the irreversible association between CH and CNF. For this purpose, the interaction between CH and uncharged CNFs were investigated by quartz crystal microbalance with dissipation monitoring (QCM-D).

Fig. 1 shows the normalized frequency ($\Delta f_n/n$) and dissipation ($\Delta D_n/n$) signals as a function of time for the successive adsorption of CNFs and CH. ($\Delta f_n/n$) shifts can be related to the change in mass of adsorbed polymers (hydrated mass) and ($\Delta D_n/n$) shifts give information on the viscoelastic properties of the adsorbed polymers. The studied concentrations and injection times of the polymer solutions were chosen according to our previous studies (Lombardo et al., 2021). Each polymer adsorption stage was followed by a rinsing step to remove excess and loosely bound polymers. Polymer adsorption was considered complete when a plateau of frequency and dissipation was reached. A layer of positively charged PAH was first deposited to facilitate the adsorption of CNFs on the gold substrate. The first CNF injection led to a decrease in frequency of –41 ± 4 Hz, evidencing the polymer adsorption. An average frequency shift between −20 and −50 Hz has been previously reported for CNF adsorption (Ahola et al., 2008; Aulin et al., 2010; de Castro et al., 2018), depending on adsorption conditions and the CNF nature. In order to demonstrate the surface saturation after each adsorption step, we injected twice CNF dispersions after the rinsing step to guarantee that no more CNFs were adsorbed. The signals of frequency and dissipation in Fig. S1 remained unchanged after the second CNF injection, meaning that the maximum CNF adsorption was reached during the first stage. Then, when CH was adsorbed on the CNF layer, the frequency decreased to –54 ± 4 Hz, and the dissipation increased to about $(17 \pm 2)\cdot10^{-6}$ units (Fig. 1). During the rinsing step, the change from 0.1 M HCl to water resulted in an increase in frequency signal and dissipation during the five first minutes. Then, the frequency remained stable at -43 ± 9 Hz while the dissipation signal decreased until attaining stability. This type of signal can be associated with the phenomenon of dewatering occurring when CH is subjected to pH changes and the binding is entropy-driven (Leray et al., 2022; Lombardo et al., 2021; Lombardo & Thielemans, 2019). The subsequent injection of CNF on the CH layer resulted in a frequency decrease at –70 ± 10 Hz, which demonstrated the irreversible adsorption of CH on the first CNF layer, which allowed the adsorption of the second CNF layer.

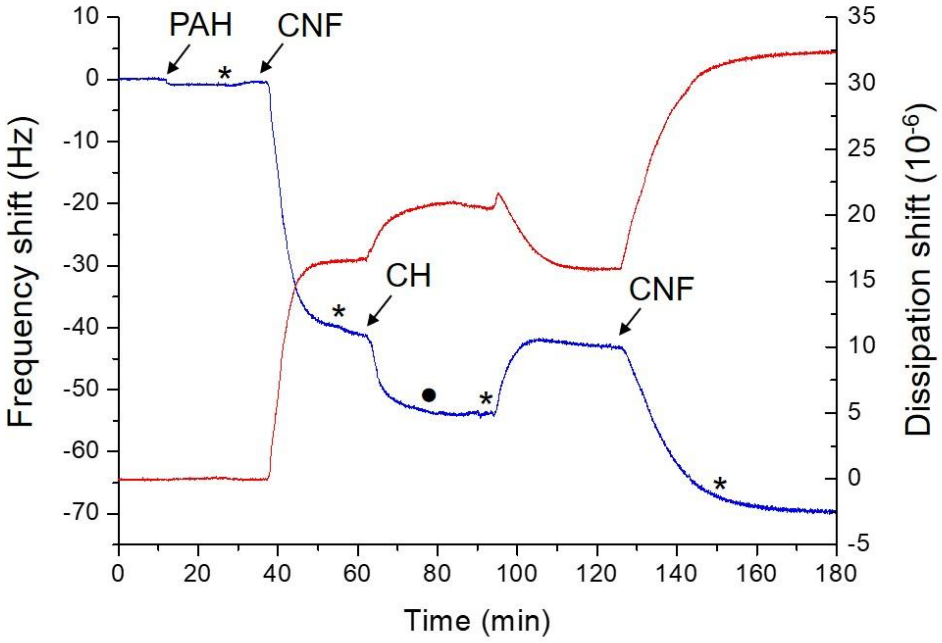

Fig. 1. $\Delta f_n/n$ and $\Delta D_n/n$ changes for the third overtone during the adsorption of CNFs and CH on the gold surface of the QCM-D sensor as a function of time. Arrows indicate the injection of the polymers and the asterisks or points indicate the rinse steps in between with water or 0.1 M HCl, respectively.

Once demonstrated the association between CNFs and CH, in order to design CH-CNF films with the optimal loading of CH, we prepared mixtures of CH (1 g·L^{-1}) and CNFs (2.5 g·L^{-1}) at different weight ratios: 5, 10, 20, 30, and 40% *wt* of CH (CH05%, CH10%, CH20%, CH30%, and CH40%, respectively). We prepared CH-CNF films by vacuum filtration following the protocol in section 2.4. When the CH concentration was above 50% *wt*, the films were stickered to the membrane hindering their potential use. Films exhibited average thicknesses of 24 ± 4 µm with an apparent density of 0.77 ± 0.01 g·cm^{-3}. A film of only pristine CH (CH100%) was prepared by casting for comparison with the CH-CNF films. Firstly, films were examined by ATR-FTIR to demonstrate that CH was not eluted from the CNF matrix during the filtration.

ATR-FTIR spectra of films are presented in Fig. 2a-b. In Fig. 2a, the CNF film spectrum displayed bands at 3500-3300 cm^{-1} (-O-H stretching vibration), 2874-2922 cm^{-1} (C-H stretching), 1634 cm^{-1} (adsorbed water), 1380 cm^{-1} (CH_3 deformation), and 1150-1085 cm^{-1} (ether bonding) (Oh et al., 2005; Schwanninger et al., 2004). CH100% film spectrum differed from CNF due to remarkable bands at 1630 cm^{-1} (C=O, amide I), 1555 and 1516 cm^{-1} (N-H deformation) (Da Róz et al., 2010; Rosca et al., 2005) (Fig. 2a). The exact position of these three peaks was determined by deconvolution of the broad band between 1800 and 1450 cm^{-1} (Fig. S2). For CH05% and CH10%, the bands corresponding to the amide groups from CH were slightly detected, probably due to a low CH concentration (Fig. 2b). Starting from the CH20% spectrum, a band at 1536 cm^{-1} indicated the presence of CH in the film, corresponding to the merging of the two N-H bands at 1555 and 1516 cm^{-1} (Fig. 2a-b). A peak fitting between 1800 and 1450 cm^{-1} was done to quantify the evolution of the band area at 1536 cm^{-1}. Fig. S2 and Table S1 report the peak fitting of the CH20%, CH30%, and CH40%; and the respective results. An area of 0.62 was obtained for CH20%; then was amplified for CH30%, with a value of 0.96; and finally, for CH40%, the band decreased to a similar area to CH20% (band area of 0.46) (Fig 2b). In all cases, the band associated with the C=O stretching from the amide group at 1630 cm^{-1} was overlapped

with the band of adsorbed water at 1634 cm^{-1} (Zhao et al., 2020). ATR-FTIR results suggested that, at a CH loading above 30%, excess CH was not retained by the CNFs during filtration and was eluted through the membrane. This result was consistent with the limitations encountered during film preparation at CH content above 50% *wt* by vacuum filtration.

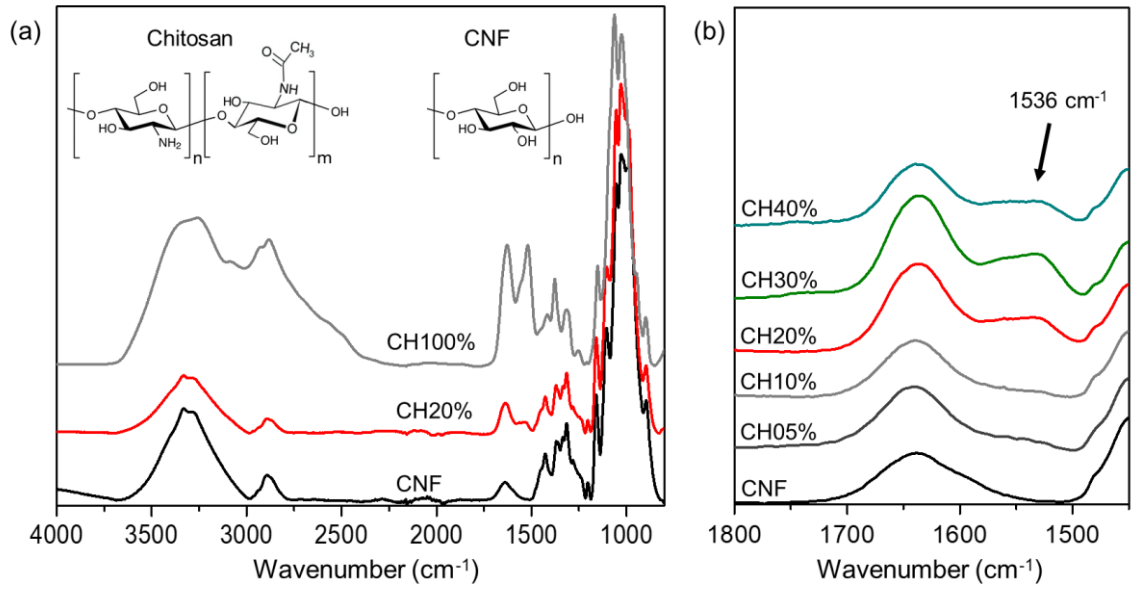

Fig. 2. (a) ATR-FTIR spectra of CNF, CH20%, CH100% films and molecular structures of CH and CNF. (b) ATR-FTIR spectra of CNF, CH05%, CH10%, CH20%, CH30%, CH40% and CH100% films in the 1800 – 1450 cm^{-1} region. The whole spectra are presented in Fig. S3.

The CH20% film was selected for the fabrication of actuators to prevent CH loss during film preparation. To get more insight into the composition of the CH20% film, the atomic percentage of carbon (%C), hydrogen (%H), and nitrogen (%N) of the CNF, CH100%, and CH20% films were measured by elementary analysis. The percentage of CH (*%CH*) in the film could be calculated as the ratio between the %N of CH20% and CH100% films:

$$\%CH = \frac{\%N_{CH20\%\ film}}{\%N_{CH100\%\ film}} 100 \qquad (4)$$

Table 1 shows the results of the elementary analysis. The CNF film was composed of 40.9 %C and 6.2 %H, and witnessed any presence of nitrogen in agreement with the composition of cellulose (Kulpinski et al., 2022; Missoum et al., 2012). The CH film also fitted the common values with 5.3 %N, 30.8 %C, and 5.8 %H (Gupta & Jabrail, 2006; Qian et al., 2018; Sarwar et al., 2015). In the CH20% film, 0.83 %N was detected asserting the successful CH incorporation within the film during film preparation. Therefore, a %CH of 15.6 ± 0.1 % was obtained which correlated well with the theoretical value of 20% CH.

Table 1. Elemental analysis results of CNF, CH100%, and CH20% films.

	CNF	CH100%	CH20%
%C	40.9 ± 0.0	30.8 ± 0.2	39.8 ± 0.2
%H	6.2 ± 0.0	5.8 ± 0.7	6.3 ± 0.0
%N	0.0 ± 0.0	5.3 ± 0.0	0.8 ± 0.1

The protonation of the amino groups of CH20% films in response to pH was monitored by ATR-FTIR. Fig. 3a shows the ATR-FTIR spectra of CH20% films at pH 2 and 12. The whole spectra are shown in Fig. S4. The deprotonation of the amino groups from CH was demonstrated by the shift from 1543 cm^{-1} to 1574 cm^{-1} of the band corresponding to the N-H deformation. Then, the CH20% film at different pHs was observed by confocal laser scanning microscopy (CLSM) to evaluate the distribution of CH within the film depending on pH. CH was labeled with rhodamine B isothiocyanate (RBITC-CH) and was mixed with the CNF dispersion to prepare RBITC-CH mixed CNF at 20% *wt* (RBITC-CH20%). Then, films were prepared following the same procedure as described above. Fig. 3b-e shows CLSM images of the film after vacuum filtration and when the films are immersed in different pH solutions. For the starting dry film, a homogenous distribution of CH was observed (Fig. 3b). When the film was immersed at pH 7 (Fig. 3c), the distribution profile changed compared to the starting film, and a network of CH aggregates appeared. Then, at pH 2 (Fig. 3d), the distribution pattern observed at pH 7 was amplified, and the film showed regions with a high CH concentration (highly colored) and regions with low CH content. Surprisingly, when the film was at pH 12 (Fig. 3e), the CH distribution seemed more homogeneous with a similar pattern to the dry film. We hypothesized that under acid conditions, CH is highly swollen, as the QCM-D results suggested, so it can diffuse within the CNF network creating a second network that expanded due to electrostatic repulsion between amino groups. Differently, under alkaline conditions, CH shrinks, and the layer dewaters forming aggregates that provide a more compacted structure. This was confirmed by the dissipation decrease when the CH layer was rinsed with water (Fig. 1). Therefore, CH20% film exhibited strong structural changes depending on the pH.

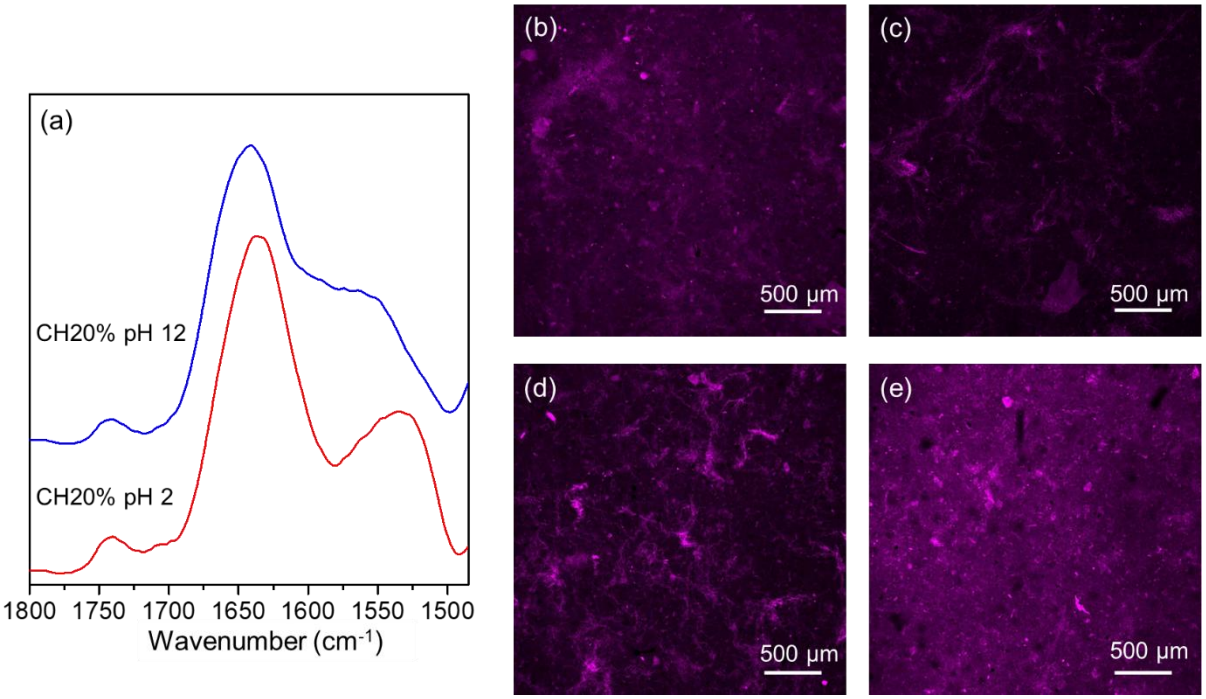

Fig. 3. (a) ATR-IR spectra of CH20% film after immersion at pH 2 and 12 in the 1800 – 1450 cm^{-1} region. The whole spectra are presented in Fig. S4. Confocal images of RBITC-CH20% film after vacuum filtration (b), and wet state for different pH values (c) 7, (d) 2, and (e) 12.

3.2. Reversible actuation of bilayer films controlled by CH and charge CNFs

We fabricated bilayer films combining a first layer of CH20% and a second layer of CNFs or carboxymethylated CNFs (CMCNFs). Two molar ratios between MCA and AGU (MCA/AGU: 0.50, and 0.70) were investigated to achieve different degrees of substitution (DS) based on a calibration curve performed in previous studies (Lopes da Costa et al., 2023). The DS were determined by conductometric titration following equation (2) (a representative titration curve is presented in Fig. S5). CMCNFs with DS of 0.10, and 0.20 (CMCNF10, and CMCNF20) were obtained for the respective MCA/AGU ratios of 0.50, and 0.70. CMCNF20 formed very stable dispersions so it was mixed at 80% *wt* with CNFs to avoid film dispersion in aqueous media. The CH20%/CNF film exhibited an average thickness of 34 ± 2 µm with an apparent density of 0.71 ± 0.05 $g \cdot cm^{-3}$, whereas the CH20%/CMCNF films showed an average thickness of 28 ± 5 µm with an apparent density of 0.75 ± 0.07 $g \cdot cm^{-3}$.

Fig. 4a-c shows the actuation performance of the CH20%/CNF and CH20%/CMCNF films under pH changes. The films were first immersed for 10 min at pH 12 (NaOH 0.01M), then 5 min at pH 2 (HCl 0.01M), and back to pH 12 for 20 min. In Fig. 4a, the CH20%/CNF film bent with the CH20% layer on the outside at pH 12. The presence of CH in the CH20% layer already entailed a difference in water uptake between the CH20% and CNF layers at high pH, and subsequently a differential expansion within the film. Then, the immersion of the CH20%/CNF film in the pH 2 solution resulted in twisting, because of higher expansion of the CH20% layer. The protonation of the amino groups from the CH20% layer created repulsions between the positively charged groups, further enhancing the difference in water uptake and expansion between CH20% and CNF layers. Back to pH 12, the CH20%/CNF film did not show any change from low pH, and the film remained twisted. Now in their basic form, the amino groups should induce a layer shrinkage, however, the shape recovery did not operate.

Differently, when CH20% was combined with CMCNFs, the presence of carboxymethyl groups influenced the behavior (Fig. 4b and c). The expansion of CH20% and CMCNF layers at the different pH was illustrated in Fig. S6. CH20%/CMCNF10 and CH20%/CMCNF20 bent with the CMCNF layer on the outside at pH 12. The carboxylic acid groups were deprotonated, creating the electrostatic repulsion between negative charges within the CMCNF layer, which yielded the layer expansion and the film bending. Moreover, CH20%/CMCNF20 was more bent than CH20%/CMCNF10, as the DS increased. The inverse mechanism was noted at pH 2 in which the CH20% layer is on the bending outside; in this case, due to the protonation of the amino groups. Back to pH 12, CH20%/CMCNF10 reached an almost straight shape while CH20%/CMCNF20 achieved complete backward movement to the other side. This meant that the difference in water uptake between CMCNF10 and CH20% layers was not sufficient to fully reverse bending compared to CH20%/CMCNF20. Therefore, the DS was revealed to be a critical parameter influencing the reversible actuation.

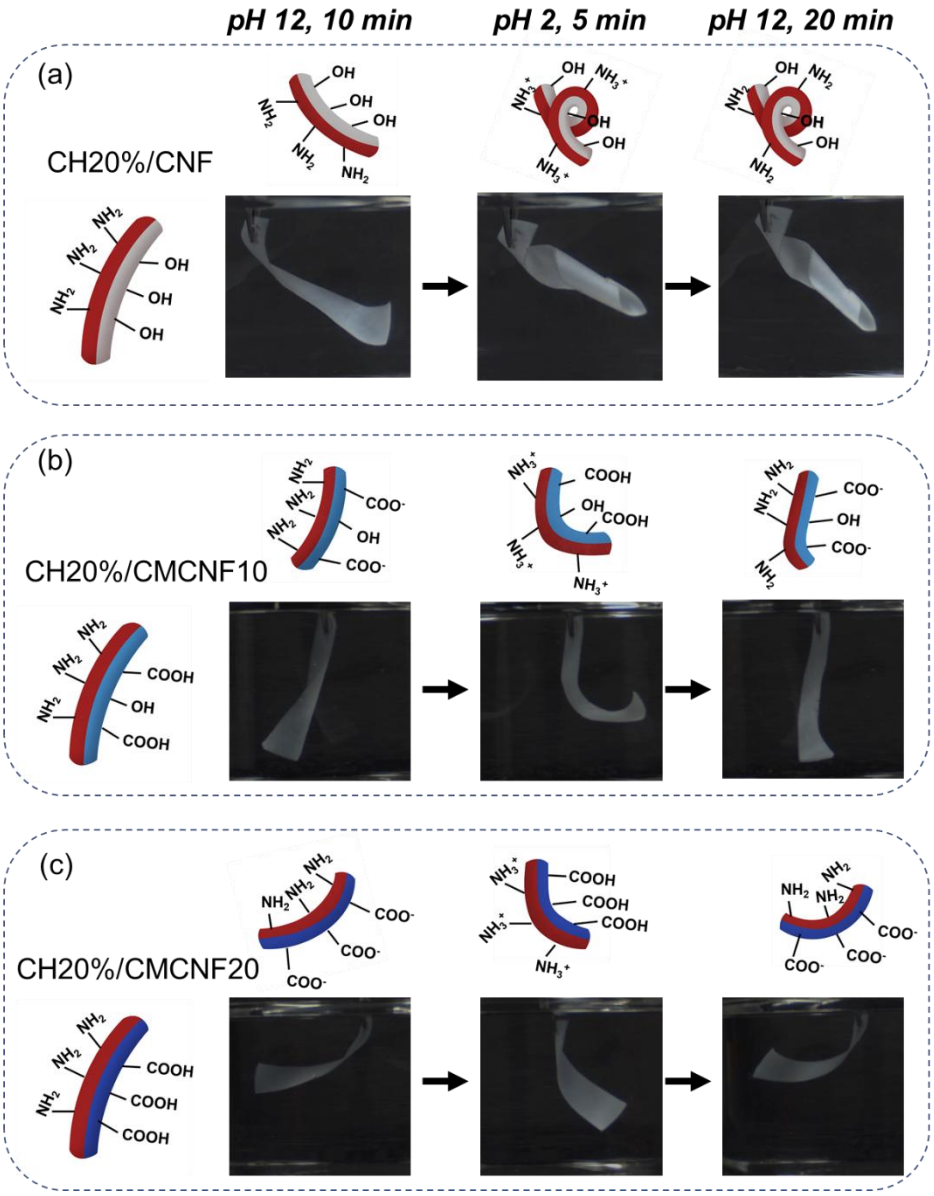

Fig. 4. Photographs showing the actuation tests under pH changes of (a)CH20%/CNF, (b) CH20%/CMCNF10, and (c) CH20%/CMCNF20 films.

To give more insight into the mechanism of actuation, the swelling of each layer was studied by fabricating single-layer films of CH20%, CNF, or CMCNFs. Swelling ratios (SW) of single-layer films immersed at pH 2, 7, and 12 are reported in Fig. 5a. Comparing CH20% and CNF films, the difference in SW turned out to be weak. In neutral and basic conditions, CH20% and CNF films had an average SW of 3.4 ± 0.4 and 2.4 ± 0.2, respectively. A slightly greater difference was obtained at pH 2 (SW of 4.0 ± 0.5 for CH20% and 2.0 ± 0.4 for CNF films). As the CH20% film had in any case a superior SW than the CNF film, which justified that bending only occurred with the CH20% layer on the outside. Moreover, this fact explained the difficulty in achieving shape recovery at pH 12 after film twisting at pH 2. Regarding the CMCNF films, the water uptake depended on the number of carboxymethyl groups on the cellulose surface. CMCNF10 film showed higher water uptakes, compared to the CNF film, but still a low dependency on pH (average SW of 3.4 ± 0.2). Differently, CMCNF20 film displayed an increasing water uptake from pH 2 to 12 (4.5 ± 0.5, 6.7 ± 0.4, and 8.0 ± 0.8 for pH 2, 7, and 12, respectively). Hence, the introduction of carboxymethyl groups ended up competing with the behavior of the CH20% layer. The increase in DS allowed bigger changes in SW

and thus, enabled reversible movements of the film. Therefore, when the films were again in an alkaline environment, the shape recovery can be completed only if a consequent swelling of the CMCNF layer is reached. This was the case of CH20%/CMCNF20, where both layers showed a significant difference in SW at high pH.

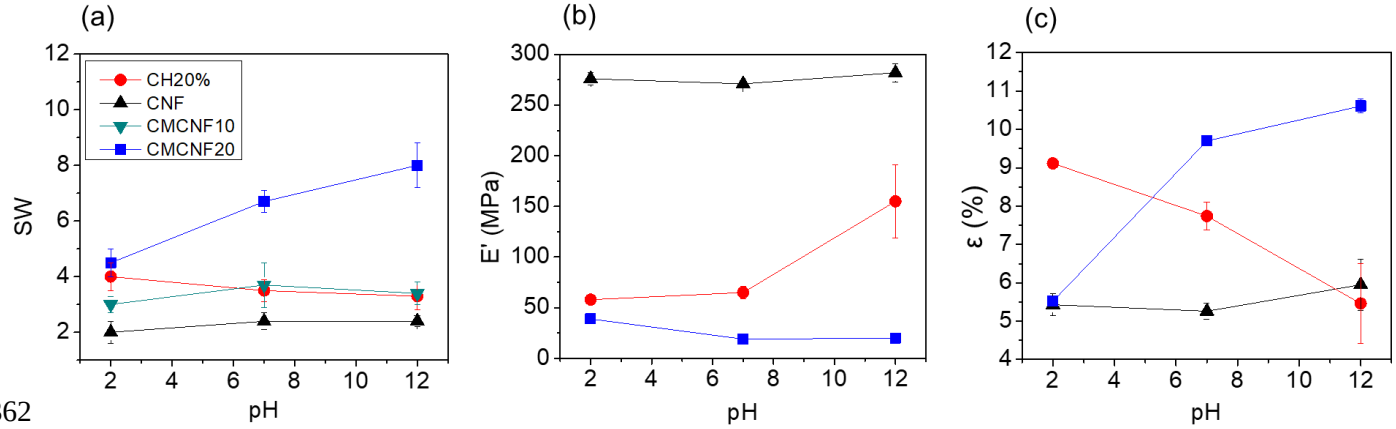

Fig. 5. (a) SW of single-layer CH20%, CNF, CMCNF10, and CMCNF20 films. (b) E' and (c) ε of single-layer CH20%, CNF, and CMCNF20 films as a function of pH.

Dynamic mechanical analysis (DMA) measurements were conducted on the single-layer CH20%, CNF, and CMCNF20 films to provide more detailed information on the changes in mechanical properties of layers at the different pHs. The storage modulus (*E'*) of the films was recorded as a function of pH (Fig. 5b). The CNF film presented relatively the same mechanical properties for all the studied pHs, with an average *E'* of 276 ± 4 MPa in agreement with previous studies (Lopes da Costa et al., 2023). The CH20% film displayed lower *E'* when immersed in aqueous solutions and an increase at high pH (*E'* of 58 ± 2 MPa, 65 ± 6 MPa, and 155 ± 36 MPa for pH 2, 7, and 12, respectively). It has been reported that the incorporation of CH enhanced water uptake within the film destroying interfibrillar hydrogen bonding (Wu et al., 2020), which justified the lower *E'* values of CH20% compared to CNF. The differences in *E'* determined the reversibility of bending upon pH changes. Thus, the lower *E'* of the CH20% layer facilitated its expansion compared to the CNF layer, and thus drove the bending of the CH20%/CNF film. However, the higher stiffness of the CNF layer prevented the shape recovery. Regarding the CMCNF20 film, *E'* was significantly lower compared to the CNF film (average *E'* of 26 ± 6 MPa). The introduction of carboxymethyl groups drastically changed the cellulose-water interaction, which resulted in a lower stiffness. Moreover, this indicates that both layers of the CH20%/CMCNF20 film displayed low *E'*. At pH 12, the CMCNF20 layer was less rigid than the CH20% layer, which facilitated the reversibility. Thus, flexibility is a key factor influencing the reversibility properties of the films.

DMA measurements also allowed the determination of changes in the film length (ε) upon immersion in the liquid (Fig. 5c). CNF layer presented low ε regardless of pH (average ε of 5.5 ± 0.3 %). The CH20% layer showed a strong decreasing ε from pH 2 to 12 (ε of 9.1 ± 0.0 %, 7.7 ± 0.4 %, and 5.5 ± 1.0 % for pH 2, 7, and 12, respectively). Inversely, CMCNF20 film exhibited increasing ε from pH 2 to 12 (5.5 ± 0.0 %, 9.7 ± 0.0 %, and 10.6 ± 0.2 % for pH 2, 7 and 12, respectively). These changes in dimension reflected the actuation behavior of the different bilayer films. Especially for the change from pH 2 to 12, a strong difference in ε at pH 2 for both couples is noted (CH20% & CNF and CH20% & CMCNF20) while, at pH 12, only CH20% and CMCNF20 layers exhibited a significant difference in ε.

This work demonstrates that polysaccharides can be combined into bilayer films to achieve pH-responsive movement. The presence of charged groups, negative carboxymethyl or positive amino groups, increases the water uptake, mainly due to the electrostatic repulsion between charges, which facilitates the separation and the interaction with water. The higher swelling also decreases the storage modulus of the charged layers compared to unmodified CNFs. Actuation can be achieved by assembling layers showing different expansions; however, reversibility requires specific mechanical properties of the layers. Therefore, actuation is not only driven by the different water uptake of each layer, higher flexibility of the expanded layer is required to achieve reversibility. The role of the storage modulus of each layer forming the film on the actuation performance has been previously described for fiber composites, and wood bilayer strips (Le Duigou et al., 2019; Rüggeberg & Burgert, 2015). Our results evidenced that, when changing the environment, the layer shrinking must provide enough rigidity to drive backward movement. Therefore, by carefully selecting key polysaccharides or combinations of them, we can tune the film bending and/or twisting, and the reversibility of the actuation.

4. Conclusion

In this work, we demonstrated that CH, unmodified, and carboxymethylated CNFs together can give rise to pH-responsive bilayer actuator films with controlled reversibility. The presence of functional groups sensitive to pH and the assembly of multilayered structures permitted to generate variations of expansion within the film responsible for shape-changing. In this case, the control of reversibility was achieved by the chemical pathway to obtain carboxylic acid groups at the CNF surface and their degrees of substitution. Functionalization opens the route to control the reversibility of pH-responsive actuators. Our results demonstrated that actuation was not only driven by water uptake but also by the mechanical properties of the layers. We provided fundamental information in terms of CH-CNF interactions, structural arrangement, swelling behavior, and mechanical properties of the different layers contributing to the mechanism of actuation. Therefore, this study enables to enhance the understanding of polysaccharides for the development of programmable materials in various applications such as soft robotics, biomedical, food, and electronic applications.

Acknowledgments

The authors gratefully thank the financial support of Région Pays de la Loire and Transform Division from the French National Research Institute for Agriculture, Food and Environment. The authors acknowledge the Bioresources, Imaging, Biochemistry, and Structure (BIBS) platform of INRAE for the access to microscopy facilities (Bruno Novales). Anne-Laure Reguerre is acknowledged for the excellent technical support for image acquisition and treatment. Denis Loquet (Nantes University) is acknowledged for his technical support in elementary analysis. We thank Borregaard for kindly providing the cellulose nanofibers.

Availability of data

The datasets generated during the current study are available from the corresponding author on reasonable request.

Conflict of interest

The authors declare that they have no known competing financial interests or personal relationships that could have appeared to influence the work reported in this paper.

References

Abdul Khalil, H. P. S., Bhat, A. H., & Ireana Yusra, A. F. (2012). Green composites from sustainable cellulose nanofibrils: A review. *Carbohydrate Polymers*, *87*(2), 963–979. https://doi.org/10.1016/j.carbpol.2011.08.078

Abitbol, T., Kloser, E., & Gray, D. G. (2013). Estimation of the surface sulfur content of cellulose nanocrystals prepared by sulfuric acid hydrolysis. *Cellulose*, *20*(2), 785–794. https://doi.org/10.1007/s10570-013-9871-0

Ahola, S., Salmi, J., Johansson, L. S., Laine, J., & Österberg, M. (2008). Model films from native cellulose nanofibrils. Preparation, swelling, and surface interactions. *Biomacromolecules*, *9*(4), 1273–1282. https://doi.org/10.1021/bm701317k

Aulin, C., Johansson, E., Wågberg, L., & Lindström, T. (2010). Self-organized films from cellulose i nanofibrils using the layer-by-layer technique. *Biomacromolecules*, *11*(4), 872–882. https://doi.org/10.1021/bm100075e

Beck, S., Méthot, M., & Bouchard, J. (2015). General procedure for determining cellulose nanocrystal sulfate half-ester content by conductometric titration. *Cellulose*, *22*(1), 101–116. https://doi.org/10.1007/s10570-014-0513-y

Cai, Z., & Kim, J. (2009). Cellulose–chitosan interpenetrating polymer network for electro-active paper actuator. *Journal of Applied Polymer Science*, *114*(1), 288–297. https://doi.org/10.1002/app.30456

Chemin, M., Beaumal, B., Cathala, B., & Villares, A. (2020). Ph-responsive properties of asymmetric nanopapers of nanofibrillated cellulose. *Nanomaterials*, *10*(7), 1–14. https://doi.org/10.3390/nano10071380

Chen, W., Sun, B., Biehl, P., & Zhang, K. (2022). Cellulose-Based Soft Actuators. *Macromolecular Materials and Engineering*, 2200072. https://doi.org/10.1002/mame.202200072

Christina, J. Y., Håkan, D., Björn, E., Norgren, L. M., Yang, J., Dahlström, Á. C., Edlund, Á. H., Lindman, Á. B., & Norgren, Á. M. (2019). pH-responsive cellulose-chitosan nanocomposite films with slow release of chitosan. *Cellulose*, *26*, 3763–3776. https://doi.org/10.1007/s10570-019-02357-5

Da Róz, A. L., Leite, F. L., Pereiro, L. V., Nascente, P. A. P., Zucolotto, V., Oliveira, O. N., & Carvalho, A. J. F. (2010). Adsorption of chitosan on spin-coated cellulose films. *Carbohydrate Polymers*, *80*(1), 65–70. https://doi.org/10.1016/j.carbpol.2009.10.062

Dawson, C., Vincent, J., & Rocca, A. (1997). How pine cone open. *Nature*, *390*(18–25), 668.

de Castro, D. O., Tabary, N., Martel, B., Gandini, A., Belgacem, N., & Bras, J. (2018). Controlled release of carvacrol and curcumin: bio-based food packaging by synergism action of TEMPO-oxidized cellulose nanocrystals and cyclodextrin. *Cellulose*, *25*(2), 1249–1263. https://doi.org/10.1007/s10570-017-1646-6

Duan, J., Liang, X., Zhu, K., Guo, J., & Zhang, L. (2017). Bilayer hydrogel actuators with tight interfacial adhesion fully constructed from natural polysaccharides. *Soft Matter*, *13*(2), 345–354. https://doi.org/10.1039/c6sm02089e

Dufresne, A. (2013). Nanocellulose: a new ageless bionanomaterial. *Materials Today*, *16*(6), 220–227. https://doi.org/10.1016/j.mattod.2013.06.004

Eichhorn, S. J., Dufresne, A., Aranguren, M., Marcovich, N. E., Capadona, J. R., Rowan, S. J., Weder, C., Thielemans, W., Roman, M., Renneckar, S., Gindl, W., Veigel, S., Keckes, J., Yano, H., Abe, K., Nogi, M., Nakagaito, A. N., Mangalam, A., Simonsen, J., … Peijs, T. (2010). Review: Current international research into cellulose nanofibres and nanocomposites. *Journal of*

Materials Science, *45*(1), 1–33. https://doi.org/10.1007/s10853-009-3874-0

Elbaum, R., Zaltzman, L., Burgert, I., & Fratzl, P. (2007). The role of wheat awns in the seed dispersal unit. *Science*, *316*(5826), 884–886. https://doi.org/10.1126/science.1140097

Erb, R. M., Sander, J. S., Grisch, R., & Studart, A. R. (2013). Self-shaping composites with programmable bioinspired microstructures. *Nature Communications*, *4*, 1–8. https://doi.org/10.1038/ncomms2666

Ganewatta, M. S., Wang, Z., & Tang, C. (2021). Chemical syntheses of bioinspired and biomimetic polymers toward biobased materials. *Nature Reviews Chemistry*, *5*(11), 753–772. https://doi.org/10.1038/s41570-021-00325-x

Gupta, K. C., & Jabrail, F. H. (2006). Effects of degree of deacetylation and cross-linking on physical characteristics, swelling and release behavior of chitosan microspheres. *Carbohydrate Polymers*, *66*(1), 43–54. https://doi.org/10.1016/j.carbpol.2006.02.019

Habibi, Y. (2014). Key advances in the chemical modification of nanocelluloses. *Chemical Society Reviews*, 43(5), 1519-1542. Royal Society of Chemistry. https://doi.org/10.1039/c3cs60204d

Huber, T., Müssig, J., Curnow, O., Pang, S., Bickerton, S., & Staiger, M. P. (2011). A critical review of all-cellulose composites. *Journal of Materials Science*, *47*(3), 1171–1186. https://doi.org/10.1007/S10853-011-5774-3

Inphonlek, S., Sunintaboon, P., Léonard, M., & Durand, A. (2020). Chitosan/carboxymethylcellulose-stabilized poly(lactide-co-glycolide) particles as bio-based drug delivery carriers. *Carbohydrate Polymers*, *242*, 116417. https://doi.org/10.1016/j.carbpol.2020.116417

Kuang, Y., Chen, C., Cheng, J., Pastel, G., Li, T., Song, J., Jiang, F., Li, Y., Zhang, Y., Jang, S. H., Chen, G., Li, T., & Hu, L. (2019). Selectively aligned cellulose nanofibers towards high-performance soft actuators. *Extreme Mechanics Letters*, *29*, 100463. https://doi.org/10.1016/j.eml.2019.100463

Kulpinski, P., Jeszka, J. K., Malolepszy, A., & Stobinski, L. (2022). Regenerated Cellulose/Graphene Composite Fibers with Electroconductive Properties. *Autex Research Journal*, *22*(2), 177–183. https://doi.org/10.2478/aut-2020-0027

Le Duigou, A., Keryvin, V., Beaugrand, J., Pernes, M., Scarpa, F., & Castro, M. (2019). Humidity responsive actuation of bioinspired hygromorph biocomposites (HBC) for adaptive structures. *Composites Part A*, *116*, 36–45. https://doi.org/10.1016/j.compositesa.2018.10.018

Leray, N., Talantikite, M., Villares, A., & Cathala, B. (2022). *Xyloglucan-cellulose nanocrystal-chitosan double network hydrogels for soft actuators*, *29*, *119753*. https://doi.org/10.1016/j.carbpol.2022.119753

Li, Q., & Renneckar, S. (2011). Supramolecular structure characterization of molecularly thin cellulose I nanoparticles. *Biomacromolecules*, *12*(3), 650–659. https://doi.org/10.1021/bm101315y

Liu, Y., Shang, S., Mo, S., Wang, P., Yin, B., & Wei, J. (2021). Soft actuators built from cellulose paper: A review on actuation, material, fabrication, and applications. *Journal of Science: Advanced Materials and Devices*, *6*(3), 321–337. https://doi.org/10.1016/j.jsamd.2021.06.004

Lombardo, S., Cathala, B., & Villares, A. (2021). Adsorption of biopolymers onto nanocelluloses for the fabrication of hollow microcapsules. *Nordic Pulp and Paper Research Journal*, *36*(4), 651–661. https://doi.org/10.1515/npprj-2021-0040

Lombardo, S., & Thielemans, W. (2019). Thermodynamics of adsorption on nanocellulose surfaces. *Cellulose*, *26*(1), 249–279. https://doi.org/10.1007/s10570-018-02239-2

Lopes da Costa, L., Moreau, C., Lourdin, D., Cathala, B., & Villares, A. (2023). Shape-recovery in

organic solvents of water-responsive cellulose nanofiber actuators. *Cellulose, submitted*.

Missoum, K., Belgacem, M. N., Barnes, J. P., Brochier-Salon, M. C., & Bras, J. (2012). Nanofibrillated cellulose surface grafting in ionic liquid. *Soft Matter*, *8*(32), 8338–8349. https://doi.org/10.1039/c2sm25691f

Moon, R. J., Martini, A., Nairn, J., Simonsen, J., & Youngblood, J. (2011). Cellulose nanomaterials review: structure, properties and nanocomposites. *Chemical Society Reviews*, *40*(7), 3941–3994. https://doi.org/10.1039/c0cs00108b

Oh, S. Y., Dong, I. Y., Shin, Y., Hwan, C. K., Hak, Y. K., Yong, S. C., Won, H. P., & Ji, H. Y. (2005). Crystalline structure analysis of cellulose treated with sodium hydroxide and carbon dioxide by means of X-ray diffraction and FTIR spectroscopy. *Carbohydrate Research*, *340*(15), 2376–2391. https://doi.org/10.1016/j.carres.2005.08.007

Qian, J., Wang, X., Shu, J., Su, C., Gong, J., Xu, Z., Jin, J., & Shi, J. (2018). A novel complex of chitosan-sodium carbonate and its properties. *Marine Drugs*, *16*(11), 1–12. https://doi.org/10.3390/md16110416

Rosca, C., Popa, M. I., Lisa, G., & Chitanu, G. C. (2005). Interaction of chitosan with natural or synthetic anionic polyelectrolytes. 1. The chitosan-carboxymethylcellulose complex. *Carbohydrate Polymers*, *62*(1), 35–41. https://doi.org/10.1016/j.carbpol.2005.07.004

Rüggeberg, M., & Burgert, I. (2015). Bio-Inspired wooden actuators for large scale applications. *PLoS ONE*, *10*(4), 1–16. https://doi.org/10.1371/journal.pone.0120718

Sarwar, A., Katas, H., Samsudin, S. N., & Zin, N. M. (2015). Regioselective sequential modification of chitosan via azide-alkyne click reaction: Synthesis, characterization, and antimicrobial activity of chitosan derivatives and nanoparticles. *PLoS ONE*, *10*(4). https://doi.org/10.1371/journal.pone.0123084

Schwanninger, M., Rodrigues, J. C., Pereira, H., & Hinterstoisser, B. (2004). Effects of short-time vibratory ball milling on the shape of FT-IR spectra of wood and cellulose. *Vibrational Spectroscopy*, *36*(1), 23–40. https://doi.org/10.1016/j.vibspec.2004.02.003

Vleugels, L. F. W., Ricois, S., Voets, I. K., & Tuinier, R. (2018). Determination of the 'apparent pKa' of selected food hydrocolloids using ortho-toluidine blue. *Food Hydrocolloids*, *81*, 273–283. https://doi.org/10.1016/j.foodhyd.2018.02.049

Wang, M., Tian, X., Ras, R. H. A., & Ikkala, O. (2015). Sensitive Humidity-Driven Reversible and Bidirectional Bending of Nanocellulose Thin Films as Bio-Inspired Actuation. *Advanced Materials Interfaces*, *2*(7), 1500080. https://doi.org/10.1002/admi.201500080

Wang, N., Chen, Y., & Kim, J. (2007). Electroactive paper actuator made with chitosan-cellulose films: Effect of acetic acid. *Macromolecular Materials and Engineering*, *292*(6), 748–753. https://doi.org/10.1002/mame.200700020

Wang, Y., Huang, W., Huang, W., Wang, Y., Mu, X., Ling, S., Yu, H., Chen, W., Guo, C., Watson, M. C., Yu, Y., Black, L. D., Li, M., Omenetto, F. G., Li, C., & Kaplan, D. L. (2020). Stimuli-responsive composite biopolymer actuators with selective spatial deformation behavior. *Proceedings of the National Academy of Sciences of the United States of America*, *117*(25), 14602–14608. https://doi.org/10.1073/pnas.2002996117

Wei, J., Jia, S., Guan, J., Ma, C., & Shao, Z. (2021). Robust and Highly Sensitive Cellulose Nanofiber-Based Humidity Actuators. *ACS Applied Materials and Interfaces*, *13*(45), 54417–54427. https://doi.org/10.1021/acsami.1c17894

Wu, M., Sukyai, P., Lv, D., Zhang, F., Wang, P., Liu, C., & Li, B. (2020). Water and humidity-induced shape memory cellulose nanopaper with quick response, excellent wet strength and folding resistance. *Chemical Engineering Journal*, *392*, 123673.

https://doi.org/10.1016/j.cej.2019.123673

Yang, L., Cui, J., Zhang, L., Xu, X., Chen, X., & Sun, D. (2021). A Moisture-Driven Actuator Based on Polydopamine-Modified MXene/Bacterial Cellulose Nanofiber Composite Film. *Advanced Functional Materials*, *31*(27), 1–11. https://doi.org/10.1002/adfm.202101378

Zhang, L., Chizhik, S., Wen, Y., & Naumov, P. (2016). Directed Motility of Hygroresponsive Biomimetic Actuators. *Advanced Functional Materials*, *26*(7), 1040–1053. https://doi.org/10.1002/adfm.201503922

Zhang, Y., Nypelö, T., Salas, C., Arboleda, J., Hoeger, I. C., & Rojas, O. J. (2013). Cellulose nanofibrils: From strong materials to bioactive surfaces. *Journal of Renewable Materials*, *1*(3), 195–211. https://doi.org/10.7569/jrm.2013.634115

Zhao, K., Wang, W., Teng, A., Zhang, K., Ma, Y., Duan, S., Li, S., & Guo, Y. (2020). Using cellulose nanofibers to reinforce polysaccharide films: Blending vs layer-by-layer casting. *Carbohydrate Polymers*, *227*, 115264. https://doi.org/10.1016/j.carbpol.2019.115264

Zhu, X., Yang, C., Jian, Y., Deng, H., Du, Y., & Shi, X. (2022). Ion-responsive chitosan hydrogel actuator inspired by carrotwood seed pod. *Carbohydrate Polymers*, *276*, 118759. https://doi.org/10.1016/j.carbpol.2021.118759